

# AN EXPERIMENTAL VALIDATION OF SPACECRAFT ATTITUDE AND POWER TRACKING WITH VARIABLE SPEED CONTROL MOMENT GYROSCOPES

Dongwon Jung\* and Panagiotis Tsiotras<sup>†</sup>

*Georgia Institute of Technology, Atlanta, GA 30332-0150*

Variable speed control moment gyros (VSCMGs) distinguish themselves from the conventional CMGs by having extra degrees of freedom to control the wheel spin in addition to the gimbal angles. Thus, they can be adopted to achieve additional objectives, such as energy storage, as well as attitude control. VSCMGs are ideal for integrated power and attitude control systems (IPACS). The gimbal rates of the VSCMGs can be used to provide the attitude control torque, whereas the wheel accelerations can be used for both attitude tracking and power tracking. Several control laws for simultaneous attitude and power tracking have been proposed in the literature. In this paper we experimentally validate an IPACS control law proposed in our previous work using a realistic 3-dof spacecraft simulator.

## Introduction

Chemical batteries onboard a spacecraft store electrical energy converted from sunlight at the solar panels during the period of exposure to the sun. When the spacecraft is in the eclipse, electric power is supplied from the chemical batteries. This causes the batteries to repeatedly charge and discharge twice over each orbit for a LEO. Since most chemical batteries have a limited number of charge and discharge cycles, the life span of the spacecraft is often decided by the life cycle of the chemical batteries. In addition, the use of chemical batteries brings about other demerits such as increased launch costs due to the large weight and sizing of the batteries, the extra care for designing a thermal protection system in order to meet the strict temperature specifications of chemical batteries, and the additional system mass for managing the charging and discharging cycles.

Rotating flywheels at high speed have been proposed as an alternative way of storing energy in lieu of chemical batteries.<sup>1</sup> These energy storage flywheels are also known as “mechanical batteries,” and they have the advantage of increased energy efficiency as well as the ability to operate at relatively high temperatures. In addition to the main attitude

---

\*Ph.D. candidate, D. Guggenheim School of Aerospace Engineering, Tel: (404) 894-6299, Email: dongwon\_jung@ae.gatech.edu.

<sup>†</sup>Professor, D. Guggenheim School of Aerospace Engineering, Tel: (404) 894-9526, Fax: (404) 894-2760. E-mail: p.tsiotras@ae.gatech.edu.

control function, flywheels also offer the possibility of combining both the energy storage and attitude control functions into a single device, hence increasing reliability and reducing the overall weight and size. This concept, known as the integrated power and attitude control system (IPACS), has been studied since the 1960s.<sup>2,3</sup> A complete survey on IPACS is given in Refs. 4 and 5. More recently, flywheels have been proposed as a viable candidate for replacing chemical batteries onboard the International Space Station (ISS).<sup>6</sup> NASA Glenn Research Center recently announced a flywheel energy storage system that achieved continuous operation at 60,000 rpm supported on magnetic bearings.

Employing flywheels for attitude control and energy storage necessitates the development of an appropriate algorithm to meet simultaneously the stringent attitude torque and the power requirements. Tsiotras et al<sup>4</sup> presented a control law for IPACS with energy/momentum wheels in an arbitrary non-coplanar configuration, whereas Roithmayr et al<sup>7</sup> developed an algorithm for the simultaneous control of both the orientation of a spacecraft and the energy stored in counter-rotating flywheels using control moment gyroscopes (CMGs). Yoon and Tsiotras<sup>8</sup> proposed control laws for IPACS using variable speed single control moment gyroscopes (VSCMGs). Although the wheel spin rates of the conventional CMGs are kept constant, the wheel spin rates of the VSCMGs are allowed to vary continuously. The benefit of the extra degrees of freedom of the acceleration commands for the spin wheels is apparent; the energy can be stored or dissipated using the wheels, while the gimbals are commanded to generate the necessary torque for precise attitude control. In Ref. 8 the authors developed both model-based and adaptive attitude and power tracking control laws (the latter for spacecraft with uncertain inertia properties), including wheel speed equalization. The numerical results of Ref. 8 showed the feasibility of employing VSCMGs for IPACS. Nevertheless, as far as the authors know, IPACS algorithms of coordinating the attitude and power tracking specifications in a seamless manner have not been validated experimentally on realistic hardware allowing full 3-dof motion.

In this paper, the IPACS of Ref. 8 is validated on a realistic three-axis spacecraft simulator. In the rest of the paper, first a brief review of the adaptive control law, the power tracking control law, and the wheel speed equalization module are summarized for the reader's convenience. A description of the experimental platform used to validate the control laws is given next. The platform is based on a realistic 3-dof spacecraft simulator equipped with four VSCMGs. The results from the experiments are given next and are compared against high fidelity numerical simulations.

## Equations of Motion

### Dynamics

The complete equations of motion for a rigid spacecraft with a cluster of  $N$  VSCMGs have been developed in the literature<sup>8</sup> and are repeated below for convenience

$$\begin{aligned} & \left( A_t [\dot{\gamma}]^d (I_{cs} - I_{ct}) A_s^T + A_s [\dot{\gamma}]^d (I_{cs} - I_{ct}) A_t^T \right) \omega \\ & + J \dot{\omega} + A_g I_{cg} \ddot{\gamma} + A_t I_{ws} [\Omega]^d \dot{\gamma} + A_s I_{ws} \dot{\Omega} + [\omega^\times] (J \omega + A_g I_{cg} \dot{\gamma} + A_s I_{ws} \Omega) = 0, \end{aligned} \quad (1)$$

where,  $\omega = (p, q, r)^T \in \mathbb{R}^3$  is the spacecraft angular velocity vector,  $\gamma = (\gamma_1, \dots, \gamma_N)^T \in \mathbb{R}^N$  is the gimbal angle vector and  $\Omega = (\Omega_1, \dots, \Omega_N)^T \in \mathbb{R}^N$  is the vector of the wheel spin

rates of the VSCMGs. All the vectors and matrices in Eq. (1) are expressed in a body-fixed frame located at the center of rotation of the spacecraft platform. For any vector  $x = (x_1, x_2, x_3)^T \in \mathbb{R}^3$ , the notation  $[x^\times]$  denotes the skew-symmetric matrix

$$[x^\times] \triangleq \begin{bmatrix} 0 & -x_3 & x_2 \\ x_3 & 0 & -x_1 \\ -x_2 & x_1 & 0 \end{bmatrix},$$

whereas, for a vector  $x \in \mathbb{R}^N$  the notation  $[x]^d \in \mathbb{R}^{N \times N}$  denotes the diagonal matrix with its elements the components of the vector  $x$ , that is,

$$[x]^d \triangleq \text{diag}(x_1, \dots, x_N).$$

In Eq. (1) the matrix  $J$  is the moment of inertia matrix of the entire spacecraft, given by

$$J \triangleq {}^B I + A_s I_{cs} A_s^T + A_t I_{ct} A_t^T + A_g I_{cg} A_g^T, \quad (2)$$

where  ${}^B I$  is the combined matrix of inertia of the spacecraft platform and the point masses of the VSCMGs. The matrices  $I_{c\star}$  and  $I_{w\star}$  are diagonal, with elements the values of the inertias of the gimbal plus wheel structure and wheel-only-structure of the VSCMGs, respectively. The  $j$ th gimbal frame of reference has unit vectors given by  $\hat{e}_{gj}, \hat{e}_{sj}, \hat{e}_{tj}$ , ( $j = 1, \dots, N$ ) along the gimbal axis, the wheel spin axis, and the torque producing axis so that  $\hat{e}_{tj} = \hat{e}_{gj} \times \hat{e}_{sj}$ , respectively. It is attached on each VSCMG and is located at the center of the gimbal/wheel combination. The matrices  $A_\star$  with  $\star = g, s$  or  $t$  then collect these unit vectors such that  $A_\star \triangleq [e_{\star 1}, \dots, e_{\star N}]$ .

## Kinematics

The modified Rodrigues parameters (MRPs) given in Refs. 9–11 are used to describe the orientation of the spacecraft. The MRPs are defined in terms of the Euler principal unit vector  $\hat{\eta}$  and angle  $\phi$ , as follows

$$\sigma = \hat{\eta} \tan(\phi/4). \quad (3)$$

The differential equation that governs the attitude kinematics in terms of the MRPs is given by

$$\dot{\sigma} = G(\sigma)\omega, \quad (4)$$

where,

$$G(\sigma) = \frac{1}{2} \left\{ \mathbf{I}_3 + [\sigma^\times] + \sigma\sigma^T - \left[ \frac{1}{2}(1 + \sigma^T\sigma) \right] \mathbf{I}_3 \right\} \quad (5)$$

and  $\mathbf{I}_3$  is the  $3 \times 3$  identity matrix.

# Attitude and Power Tracking with Wheel Speed Equalization

In this section, a control law is presented for combined attitude and power tracking using  $N$  VSCMGs. In addition, wheel speed equalization is applied for distributing the power requirement amongst the  $N$  wheels in the VSCMG cluster so that it prevents some wheels in the VSCMG cluster from possibly becoming impaired to generate torque properly due to wheel saturation or singularities.

## Adaptive Attitude Tracking with VSCMGs

The mass properties of a spacecraft are often unknown a priori. This necessitates applying an adaptive attitude control to deal with the uncertainty associated with the mass moment of inertia. Furthermore, in the VSCMG case the spacecraft inertia matrix  $J$  also depends on the gimbal angles  $\gamma$ , hence it is time-varying; see Eq. (2). Notice nonetheless that the derivative of  $J$  is known. Consequently, an adaptive control law that uses estimates of the elements of  $J$  is designed in Ref. 8 using arguments similar to standard adaptive control design techniques. The steps of Ref. 8 are summarized below.

First notice that equation (1) can be rewritten as

$$\frac{1}{2}\dot{J}\omega + J\dot{\omega} + [\omega^\times](J\omega + A_s I_{ws}\Omega) + B\ddot{\gamma} + \tilde{C}\dot{\gamma} + D\dot{\Omega} = 0, \quad (6)$$

where,

$$B = A_g I_{cg}, \quad D = A_s I_{ws}, \quad (7a)$$

$$\tilde{C} = A_t I_{ws}[\Omega]^d + [\omega^\times]A_g I_{cg} + \frac{1}{2} \left[ (e_{s1}e_{t1}^\top + e_{t1}e_{s1}^\top)\omega, \dots, (e_{sN}e_{tN}^\top + e_{tN}e_{sN}^\top)\omega \right] (I_{cs} - I_{ct}). \quad (7b)$$

Typically, the gimbal acceleration term  $B\ddot{\gamma}$  can be ignored because the matrix  $B$  is small compared to the matrices  $\tilde{C}$  and  $D$ .<sup>12</sup>

Differentiating Eq. (4), one obtains

$$\dot{\omega} = G^{-1}(\sigma)\ddot{\sigma} - G^{-1}(\sigma)\dot{G}(\sigma, \dot{\sigma})\omega. \quad (8)$$

Substituting Eq. (8) and Eq. (4) into Eq. (6) one ends up with the equation of the system written in the standard form:

$$H^*(\sigma)\ddot{\sigma} + C^*(\sigma, \dot{\sigma})\dot{\sigma} = F(\sigma, \dot{\sigma}, \gamma, \Omega, \dot{\gamma}, \dot{\Omega}) \quad (9)$$

where,

$$\begin{aligned} H^*(\sigma) &\triangleq G^{-\top}(\sigma)JG^{-1}(\sigma), \\ C^*(\sigma, \dot{\sigma}) &\triangleq -G^{-\top}(\sigma)JG^{-1}(\sigma)\dot{G}(\sigma, \dot{\sigma})G^{-1}(\sigma) - G^{-\top}(\sigma)[(J\omega)^\times]G^{-1}(\sigma), \\ F &\triangleq G^{-\top}(\sigma)[(A_s I_{ws}\Omega)^\times]\omega - G^{-\top}(\sigma)(\tilde{C}\dot{\gamma} + D\dot{\Omega}) - \frac{1}{2}G^{-\top}(\sigma)\dot{J}\omega. \end{aligned} \quad (10)$$

Note that the left-hand-side of Eq. (9) is linear in terms of the elements of  $J$ , which are the unknown parameters to be estimated. Let  $a \in \mathbb{R}^6$  be the parameter vector defined by

$$a \triangleq (J_{11}, J_{12}, J_{13}, J_{22}, J_{23}, J_{33})^\top, \quad (11)$$

and let  $\hat{a}$  be an estimate of  $a$ . The following theorem presents an adaptive attitude tracking control law. A detailed proof can be found in Ref. 8.

**Theorem 1 (Ref. 8)** *Let  $s = \dot{\tilde{\sigma}} + \lambda\tilde{\sigma} = \dot{\sigma} - \dot{\sigma}_r$  ( $\lambda > 0$ ) where  $\tilde{\sigma} = \sigma - \sigma_d$  is the attitude tracking error,  $\sigma_d$  is the reference attitude trajectory, and  $\dot{\sigma}_d$  is the derivative of the reference trajectory and  $\dot{\sigma}_r = \dot{\sigma}_d - \lambda\tilde{\sigma}$  is the reference velocity vector. Consider the following attitude control law*

$$F = \hat{H}^*(\sigma)\ddot{\sigma}_r + \hat{C}^*(\sigma, \dot{\sigma})\dot{\sigma}_r - K_D s - \frac{1}{2}G^{-\top}(\sigma)\dot{J}G^{-1}(\sigma)s \quad (12)$$

where  $\hat{H}^*(\sigma) = G^{-\top} \hat{J} G^{-1}$  and  $\hat{C}^*(\sigma, \dot{\sigma}) = -G^{-\top} \hat{J} G^{-1} \dot{G} G^{-1} - G^{-\top} [(\hat{J}\omega)^\times] G^{-1}$ ,  $K_D > 0$ , and the adaptation law

$$\dot{\hat{a}} = -\Gamma Y^{*\top} s + \dot{a} \quad (13)$$

where  $\Gamma > 0$ , and  $Y^*(\sigma, \dot{\sigma}, \dot{\sigma}_r, \ddot{\sigma}_r)$  is a known matrix satisfying

$$Y^*(\sigma, \dot{\sigma}, \dot{\sigma}_r, \ddot{\sigma}_r) \tilde{a} \triangleq \tilde{H}^*(\sigma) \ddot{\sigma}_r + \tilde{C}^*(\sigma, \dot{\sigma}) \dot{\sigma}_r, \quad (14)$$

where  $\tilde{H}^*(\sigma) = \hat{H}^*(\sigma) - H^*(\sigma)$ ,  $\tilde{C}^*(\sigma, \dot{\sigma}) = \hat{C}^*(\sigma, \dot{\sigma}) - C^*(\sigma, \dot{\sigma})$ , and  $\tilde{a} = \hat{a} - a$  is the parameter estimation error. Then the closed-loop system of Eqs. (9), (12), and (13) is globally asymptotically stable, that is,  $s \rightarrow 0$  and  $\sigma \rightarrow \sigma_d$ .

From Eqs. (12) and (9) it follows that the required control inputs are obtained by solving

$$\mathbf{Q}_a \mathbf{u} = \mathbf{L}_{ra}, \quad (15)$$

where,

$$\begin{aligned} \mathbf{Q}_a &= \begin{bmatrix} C & D \end{bmatrix}, \\ \mathbf{L}_{ra} &= -G^\top(\sigma) [\hat{H}^*(\sigma) \ddot{\sigma}_r + \hat{C}^*(\sigma, \dot{\sigma}) \dot{\sigma}_r - K_D s] + [(A_s I_{ws} \Omega)^\times] \omega, \end{aligned}$$

and

$$\begin{aligned} C &= A_t I_{ws} [\Omega]^d + [\omega^\times] A_g I_{cg} + \\ &\frac{1}{2} \left[ (e_{s1} e_{t1}^\top + e_{t1} e_{s1}^\top) (\omega + G^{-1} \dot{\sigma}_r), \dots, (e_{sN} e_{tN}^\top + e_{tN} e_{sN}^\top) (\omega + G^{-1} \dot{\sigma}_r) \right] (I_{cs} - I_{ct}). \end{aligned} \quad (16)$$

Note that the control input calculated in Eq. (15) is  $\mathbf{u} = [\dot{\gamma} \quad \dot{\Omega}]^\top$ . The gimbal motor and the spin motor in practice require torque commands instead of the gimbal rate  $\dot{\gamma}$  or the wheel spin acceleration  $\dot{\Omega}$  commands. The control law in terms of  $[\dot{\gamma} \quad \dot{\Omega}]^\top$  has to be implemented via internal feedback loops to generate the torque commands to the corresponding motors.

## Power Tracking

The total kinetic energy stored in the momentum wheels is

$$T = \frac{1}{2} \Omega^\top I_{ws} \Omega. \quad (17)$$

Hence, the power (rate of change of the energy) is obtained by

$$P = \frac{dT}{dt} = \Omega^\top I_{ws} \dot{\Omega} = \begin{bmatrix} 0 & \Omega^\top I_{ws} \end{bmatrix} \begin{bmatrix} \dot{\gamma} \\ \dot{\Omega} \end{bmatrix}. \quad (18)$$

Equation (18) is augmented to the attitude tracking steering equation (15) to obtain the augmented steering equation for the IPACS with the VSCMGs,

$$\mathbf{Q}_p \mathbf{u} = \mathbf{L}_{rp} \quad (19)$$

where,

$$\mathbf{Q}_p = \begin{bmatrix} C & D \\ \mathbf{0}_{1 \times N} & (\Omega^\top I_{ws})_{1 \times N} \end{bmatrix}, \quad \mathbf{L}_{rp} = \begin{bmatrix} \mathbf{L}_{ra} \\ P \end{bmatrix}, \quad (20)$$

and  $P$  is the desired power profile derived from the mission specifications.

## Wheel Speed Equalization

If some of the wheel speeds become too small (or zero) the required torque for attitude control cannot be produced, regardless of the gimbal rate commands. If this is the case, the remaining degrees of freedom of the VSCMG cluster may not be enough to allow exact attitude and power tracking. On the other hand, if some of the wheel speeds become too high, those wheels might saturate so that the VSCMG cluster loses the capability to track an arbitrary power profile. Desaturation of the wheels is possible by thruster firing, yet depleting valuable fuel. In order to minimize the possibility of singularity and/or wheel saturation, it is desirable to equalize the wheel speeds of the VSCMGs, whenever possible. Two methods are proposed in Ref. 8, which are briefly outlined below. The first method achieves exact wheel speed equalization for all times (hard constraint), whereas the second method achieves wheel speed equalization only when the wheel speed equalization does not interfere with the singularity avoidance task (soft constraint).

The first method in Ref. 8 adds an extra constraint that forces the wheel speeds to converge to the average wheel speed of the cluster. To this end, let the performance measure

$$\mathcal{J}_{w1}(\Omega_1, \dots, \Omega_N) = \frac{1}{2} \sum_{i=1}^N (\Omega_i - \bar{\Omega})^2 = \frac{1}{2} \Omega_e^\top \Omega_e, \quad (21)$$

where,

$$\bar{\Omega} = \frac{1}{N} \sum_{i=1}^N \Omega_i, \quad \Omega_e = \Omega - \bar{\Omega} \mathbf{1}_{N \times 1}, \quad (22)$$

and  $\mathbf{1}_{N \times 1}$  is  $N \times 1$  vector whose elements are 1s. The condition for equalization is expressed as the requirement that the rate of change of the performance measure  $\mathcal{J}_{w1}$  forms a stable dynamic system with a certain time constant. That is,

$$\frac{d}{dt} \mathcal{J}_{w1} = \nabla \mathcal{J}_{w1} \dot{\Omega} = \sum_{i=1}^N \frac{\partial \mathcal{J}_{w1}}{\partial \Omega_i} \dot{\Omega}_i = -k_2 \mathcal{J}_{w1} \quad (23)$$

where,  $k_2 > 0$ . This condition is then augmented to Eq. (19), and the control input  $\mathbf{u}$  is obtained by solving the resulting linear system. In other words, the control law that achieves attitude and power tracking with wheel speed equalization is given by

$$\mathbf{Q}_w \mathbf{u} = \mathbf{L}_{rw}, \quad (24)$$

where,

$$\mathbf{Q}_w = \begin{bmatrix} C & D \\ \mathbf{0}_{1 \times N} & (\Omega^\top I_{ws})_{1 \times N} \\ \mathbf{0}_{1 \times N} & (\nabla \mathcal{J}_{w1})_{1 \times N} \end{bmatrix}, \quad \mathbf{L}_{rw} = \begin{bmatrix} \mathbf{L}_{ra} \\ P \\ -k_2 \mathcal{J}_{w1} \end{bmatrix}. \quad (25)$$

Using the fact that  $\Omega_e = [\mathbf{I}_N - (1/N)\mathbf{1}_{N \times N}]\Omega$ , where  $\mathbf{1}_{N \times N}$  is  $N \times N$  matrix whose elements are 1s and the matrix  $[\mathbf{I}_N - (1/N)\mathbf{1}_{N \times N}]$  is idempotent, it can be easily shown that  $\nabla \mathcal{J}_{w1} = \Omega_e^\top$ .

The second wheel speed equalization algorithm seeks to minimize the following cost

$$\mathcal{J}_{w2} = \frac{1}{2} \mathbf{u}^\top \mathbf{W}^{-1} \mathbf{u} + \mathbf{R} \mathbf{u}, \quad (26)$$

where the weighting matrix  $\mathbf{R}$  is chosen so as to penalize any wheels rotating faster or slower than the average wheel speed, as follows

$$\mathbf{R} = [ \mathbf{0}_{1 \times N} \quad k_3 \Omega_e^\top ], \quad k_3 > 0. \quad (27)$$

The solution minimizing the cost in Eq. (26) is found as

$$\mathbf{u} = \mathbf{W} \left[ \mathbf{Q}_p^\top (\mathbf{Q}_p \mathbf{W} \mathbf{Q}_p^\top)^{-1} (\mathbf{L}_{rp} + \mathbf{Q}_p \mathbf{W} \mathbf{R}^\top) - \mathbf{R}^\top \right]. \quad (28)$$

In case  $\mathbf{Q}_p$  is not full rank, the following equation can be used instead

$$\begin{aligned} \mathbf{u} &= \mathbf{W}^{\frac{1}{2}} (\mathbf{Q}_p \mathbf{W}^{\frac{1}{2}})^\dagger (\mathbf{L}_{rp} + \mathbf{Q}_p \mathbf{W} \mathbf{R}^\top) - \mathbf{W} \mathbf{R}^\top \\ &= \mathbf{W}^{\frac{1}{2}} (\mathbf{Q}_p \mathbf{W}^{\frac{1}{2}})^\dagger \mathbf{L}_{rp} - \left[ \mathbf{I}_N - \mathbf{W}^{\frac{1}{2}} (\mathbf{Q}_p \mathbf{W}^{\frac{1}{2}})^\dagger \mathbf{Q}_p \right] \mathbf{W} \mathbf{R}^\top. \end{aligned} \quad (29)$$

It is worth mentioning that neither of the previous two wheel equalization algorithms conflicts with the attitude and power tracking control objectives.

### Solving the VSCMG Steering Equation

The matrices  $\mathbf{Q}_\star$  in Eqs. (15), (19), (24) have dimensions  $4 \times 2N$ ,  $5 \times 2N$ , and  $6 \times 2N$ , respectively. Whenever  $\mathbf{Q}_\star$  has maximal rank (and  $N \geq 4$ ), those equations have infinitely many solutions. The minimum-norm solution calculated from

$$\mathbf{u} = \mathbf{Q}^\dagger \mathbf{L}_{r\star} = \mathbf{Q}_\star^\top (\mathbf{Q}_\star \mathbf{Q}_\star^\top)^{-1} \mathbf{L}_{r\star}, \quad \star = a, w, p \quad (30)$$

where  $(\cdot)^\dagger$  represents the pseudo inverse, and which minimizes

$$\min_{\mathbf{u}} \|\mathbf{u}\|^2 \quad \text{subject to} \quad \mathbf{Q}_\star \mathbf{u} = \mathbf{L}_{r\star}, \quad (31)$$

is known as the Moore-Penrose (MP) solution.<sup>13</sup> On the other hand, if the  $C$  matrix in Eqs. (15), (19), (24) is rank deficient so is the matrix  $\mathbf{Q}_\star$ . Consequently, no exact solution that satisfies Eq. (31) exists, unless  $L_{r\star}$  is in the range space of  $\mathbf{Q}_\star$ . The matrix  $\mathbf{Q}_\star \mathbf{Q}_\star^\top$  is not invertible and the steering law Eq. (30) fails to achieve simultaneous attitude and power tracking control except for very special cases.<sup>4</sup>

Although the rank deficiency of the  $C$  matrix can be alleviated using more VSCMGs, the possibility of the singularity still remains. Moreover, the MP solution tends to steer the gimbals towards the rank deficient configurations.<sup>13,14</sup> Several methods have been proposed to keep the matrix  $C$  full rank,<sup>15-17</sup> and compared experimentally on a 3-dof spacecraft simulator.<sup>18</sup>

It is advantageous for the VSCMGs to act as conventional CMGs to produce the most torque from the torque amplification effect, which is a significant merit of the CMGs. If the VSCMG cluster approaches towards a singularity, however, it is favorable for the VSCMGs to act as momentum wheels (MWs) to avoid singularities. A weighted minimum-norm solution, which minimizes the weighted cost

$$\mathcal{J}_2 = \frac{1}{2} \mathbf{u}^\top \mathbf{W}^{-1} \mathbf{u} \quad (32)$$

can be used to switch the VSCMGs between CMG and MW modes.<sup>12,16</sup> Defining the weighting matrix  $\mathbf{W}$  as follows

$$\mathbf{W} = \begin{bmatrix} w_1 e^{-w_2 \sigma_c} \mathbf{I}_N & \mathbf{0}_N \\ \mathbf{0}_N & \mathbf{I}_N \end{bmatrix}, \quad (33)$$

where,  $\mathbf{I}_N$  is the  $N \times N$  identity matrix and  $\sigma_c$  is the condition number of  $C$  (the ratio of the largest to the smallest singular value) and  $w_1$  and  $w_2$  are positive gains chosen by the user, the weighted minimum-norm solution is obtained by

$$\mathbf{u} = \mathbf{W} \mathbf{Q}_*^T (\mathbf{Q}_* \mathbf{W} \mathbf{Q}_*^T)^{-1} \mathbf{L}_{r*}. \quad (34)$$

In case  $\mathbf{Q}_*$  is not full row rank, the approximate solution can be obtained from

$$\mathbf{u} = \mathbf{W}^{\frac{1}{2}} (\mathbf{Q}_* \mathbf{W}^{\frac{1}{2}})^\dagger \mathbf{L}_{r*}. \quad (35)$$

From the solution Eq. (34) with the weighting matrix  $\mathbf{W}$ , it can be ascertained that the VSCMGs can operate either in MW mode ( $\|\dot{\Omega}\| < \|\dot{\gamma}\|$ , when  $\sigma_c$  is small) or in regular CMG mode ( $\|\dot{\Omega}\| > \|\dot{\gamma}\|$ , when  $\sigma_c$  is large) depending on the singularity measure  $\sigma_c$ . As a singularity is approached, the VSCMGs will smoothly switch to MW mode to avoid the singularity. The VSCMGs will switch back to the CMG mode whenever they are far away from any singularities. Thus, the weighted minimum-norm solution can manage temporary rank deficiencies of the matrix  $C$ .

## Description of Experimental Facility

### The Georgia Tech 3-dof Spacecraft Platform

The experimental facility which was used to implement the attitude and power tracking control law of the previous section is based on a three-axial air bearing, located at the Dynamics and Control Systems Laboratory of the School of Aerospace Engineering at the Georgia Institute of Technology, shown in Fig. 1. The facility provides three rotational degrees of freedom as follows:  $\pm 30$  deg about  $x$  and  $y$  axes (horizontal) and 360 deg about the  $z$  axis (vertical). It was designed to support advanced research in the area of nonlinear spacecraft attitude dynamics and control.

The spacecraft platform is made of a cylindrical aluminum structure, and it is equipped with a variety of actuators and sensors: a set of cold-gas thrusters, four variable-speed control moment gyros, a two-axis sun sensor, a three-axis magnetometer, a three-axis rate gyro, and an inertial measurement unit (IMU). An onboard computer and wireless ethernet connection with the host computer allow high-speed communication and real-time implementation of control algorithms.

### VSCMG Actuators

For the experiments presented in this paper the VSCMG actuators were employed to provide the necessary torque on the spacecraft, while imitating the behavior of mechanical batteries through spinning up and spinning down of the wheels. There are four VSCMG modules on the spacecraft platform, mounted in a pyramid configuration with a skew angle of 54.7 deg.



Figure 1. The Georgia Tech three-axial spacecraft simulator.

One of the VSCMG modules is shown in Fig. 2. Each VSCMG module has two brushless DC motors. One of the motors controls the gimbal, while the other controls the spin wheel. A potentiometer measures the rotation angle of the gimbal. The gimbal rate signal is also available to the user via a separate I/O channel. The gimbal motor operates in gimbal rate mode via an internal PID servo loop torquing the gimbal according to a gimbal rate command. The gimbal is allowed to rotate within  $\pm 100$  deg and the maximum achievable gimbal rate is limited to  $\pm 25$  deg/sec. The spin wheel motor is coupled directly (no gearbox) to a momentum wheel, and it operates according to a torque command. The maximum torque output of the wheel motor is 310 mNm, and it saturates at a maximum speed of 4000 rpm. In CMG mode, the wheel motor operates at a constant speed via an internal PID servo loop according to a specified angular momentum magnitude. An incremental digital encoder with resolution of 500 pulses per revolution is coupled to the spin axis to capture the angular position of the wheel. The spin rate is made available to the user by differentiating the angular displacement at a sampling rate of 100 Hz. In torque mode the wheel acceleration can be controlled via an additional PID loop from the measurement of the spin rate.

The maximum acceleration/deceleration of the wheel is  $73 \text{ rad/sec}^2$  with a moment of inertia of the wheel  $I_{ws} = 0.0042 \text{ kg-m}^2$ . Hence, the maximum power that can be ideally extracted from a spinning wheel is

$$\begin{aligned}
 P_{\max} &= \Omega_{\max} I_{ws} \dot{\Omega}_{\max} \\
 &= 419 \times 0.0042 \times 73 = 128 \text{ Watt},
 \end{aligned}
 \tag{36}$$

where  $P_{\max}$  is the instantaneous power delivered from the spinning wheel to the system. The detailed physical data of each VSCMG are listed in Table 1.

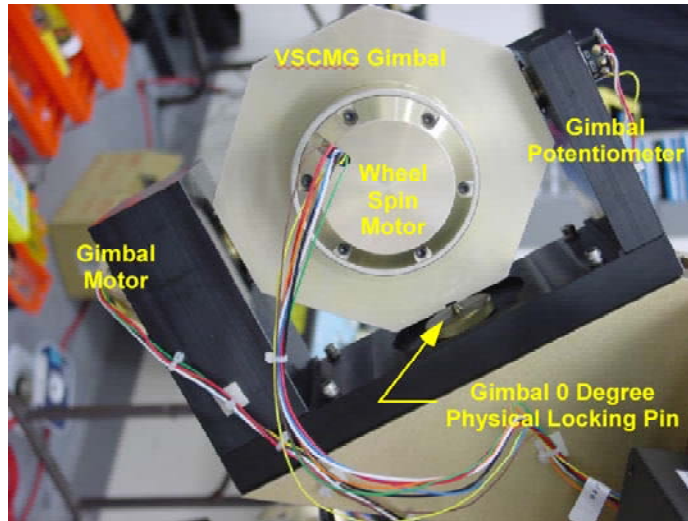


Figure 2. Main components of the VSCMG module.

## Communication, Computer and Electronics

An industrial embedded computer (ADLink NuPRO-775 Series) is used for data acquisition, data recording, and control law implementation via the MATLAB xPC Target Environment<sup>®</sup> with Embedded Option.<sup>19</sup> The main CPU is based on the Intel Pentium<sup>®</sup> III 750MHz processor with on-board memory 128MB DRAM and 128MB disk-on-chip, allowing the user for real-time data acquisition, processing, and data recording. The connection to a host computer is achieved in the xPC Target Environment via a wireless ethernet LAN connection. A wireless LAN router (DLink DI-713P) and a USB adapter (DLink DWL-120) allow to transfer data at speeds up to 11 Mbps.

The target computer system has three data acquisition interface cards. Two analog input cards (PCI-6023E from National Instruments) are used to measure the analog voltages from the rate gyro, magnetometer, sun sensor, and so on. Another analog output card (PCI-6703 from National Instruments) is used to control the VSCMGs.

A detailed description of the design and construction of this experimental spacecraft simulator facility, including specifications for all sensors and actuators can be found in Ref. 20.

## Experimental Results

In this section we present the results from the experimental validation of the adaptive attitude and power tracking control law presented earlier and we compare the results against numerical simulation using a high fidelity model. A power profile similar to that given in Ref. 8 was chosen as a reference to track. The power profile is scaled down so that the peak power is 15 Watt. For implementation purposes we need to take into account the angle limits of the air bearing in roll and pitch, so we have chosen the reference attitude trajectory in terms of Eulerian angle as follows

$$[ \phi_d(t) \quad \theta_d(t) \quad \psi_d(t) ] = [ \pi/36 \sin(\pi t/25) \quad 0 \quad \pi/6 \sin(\pi t/50) ] \text{ rad.}$$

**Table 1. VSCMG Physical Data.**

Item	Value	Units
$I_{ws}$	diag[0.0042, 0.0042, 0.0042, 0.0042]	kg-m <sup>2</sup>
$I_{cs}$	diag[0.0146, 0.0146, 0.0146, 0.0146]	kg-m <sup>2</sup>
$I_{cg}$	diag[0.0082, 0.0082, 0.0082, 0.0082]	kg-m <sup>2</sup>
$I_{ct}$	diag[0.0121, 0.0121, 0.0121, 0.0121]	kg-m <sup>2</sup>
Pyramid skew angle	54.7	deg
Maximum wheel speed	4000	rpm
Peak torque of the spin motor	310	mNm
Gimbal angle range	±100	deg
Gimbal rate limit	±25	deg/sec

Since the MRPs are utilized in the adaptive tracking control law, we need to transform this representation to the MRPs according to the transformation given in Ref. 9.

Simulation studies were first conducted to validate the IPACS algorithm by taking the actual hardware constraints into consideration. A high fidelity Simulink<sup>®</sup> model of the entire spacecraft dynamics including details of all subsystems was utilized to find appropriate gains for the IPACS control algorithm. After several trials the control gains were finally chosen as follows

$$K_D = 3 \times 10^2 \cdot \mathbf{I}_3, \quad \Gamma = 1 \times 10^4 \cdot \mathbf{I}_6, \quad \lambda = 0.1,$$

$$k_2 = k_3 = 0.3, \quad w_1 = 0.01, \quad w_2 = 0.01.$$

For the initial setup for the experiments the wheels were spun up to

$$\Omega(t_0) = [2, 2.2, 2.8, 3]^\top \times 10^3 \text{ rpm}$$

and the initial gimbal angles were set to zero. This was done in order to enable the VSCMGs to produce the required control torque magnitude and also to test the wheel speed equalization algorithm. In addition, the spacecraft platform was initially at rest in a configuration close (but not equal) to the reference trajectory.

Three sets of experiments were conducted. In the first experiment, no wheel speed equalization algorithm was used. The objective was only to track the reference attitude and power profiles. In the second set of experiments the first wheel speed equalization algorithm of the previous section was implemented, while in the third set the second wheel speed equalization algorithm was implemented. For all cases, the results from the experiments were compared with numerical predictions.

Figures 3-8 show the results from the first set of experiments. Specifically, Figure 3 shows the actual attitude histories compared with the reference attitude histories. The spacecraft succeeds in following the reference attitude over the entire period of the maneuver. Figure 4 shows the attitude error in terms of the Eulerian angles. The maximum angle error is approximately 1 deg. This small discrepancy from the reference is attributed to the neglected constant gravity torque arising from the misalignment between the center

of mass of the platform and its center of rotation. This torque deteriorates the tracking performance affecting mainly the pitch and roll axes as is clearly evident in Figure 4. This error can be reduced or eliminated by either an additional integral action in the control loop or explicit cancelation of the gravity torque by the controller (see Ref. 18). Figure 5 shows the actual versus the commanded power profile. The two agree very well, confirming the successful operation of coordinated attitude and power tracking. The corresponding wheel speeds are shown in Figure 6. The wheels spin-up to store energy (positive power) and despin to discharge energy (negative power). In all the previous figures also note the very close correlation between the experimental results and the numerical simulations. The gimbal angles, the control commands (gimbal rate  $\dot{\gamma}$  and wheel acceleration  $\dot{\Omega}$ ) are shown in Figure 7. The results from the numerical simulation for the gimbal angles, the gimbal rates and the wheel accelerations are shown in Figure 8. Comparison of Figures 7(a) and 8(a) shows some discrepancy between the predicted and the actual gimbal angle history. This can be attributed to the somewhat different (albeit small) actual commanded angular rate during the experiments due to the gravity torque. Since the gimbal angles are somewhat different, the condition number of the matrix  $C$  during the experiment (shown in Figure 7(d)) also differs from the condition number predicted from the numerical simulations (shown in Figure 8(d)). In both cases, however, the results are very similar and certainly within the same order of magnitude. The condition number remains bounded, which implies that no singularity has been encountered during the maneuver.

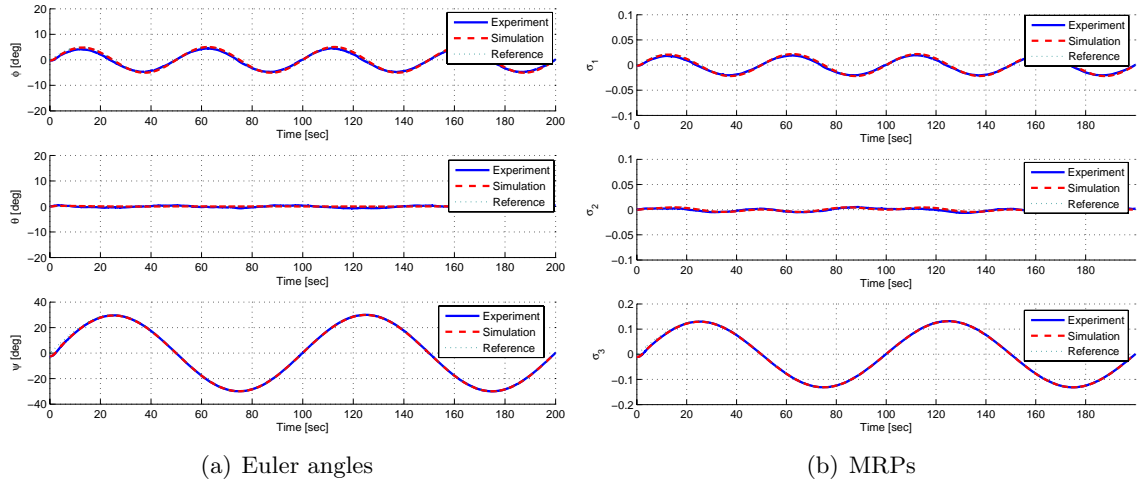


**Figure 3. Experimental and simulated results for attitude history without wheel speed equalization.**

The results from the second set of experiments are shown in Figures 9-14. Specifically, Figure 9 shows the actual attitude histories compared with the reference attitude trajectories, whereas Figure 10 shows the attitude error in terms of the Eulerian angles. Figure 11 shows the actual power profile versus the required power reference along with the simulated power trajectory. All agree extremely well. Most interesting for this set of experiments is perhaps Figure 12, which shows the wheel speed histories. With the wheel speed equalization algorithm engaged, the wheel speeds tend to the same value after an initial transient. This has been achieved without any deterioration in the attitude and power tracking performance. Finally, the gimbal angles, the control commands, and the condition number

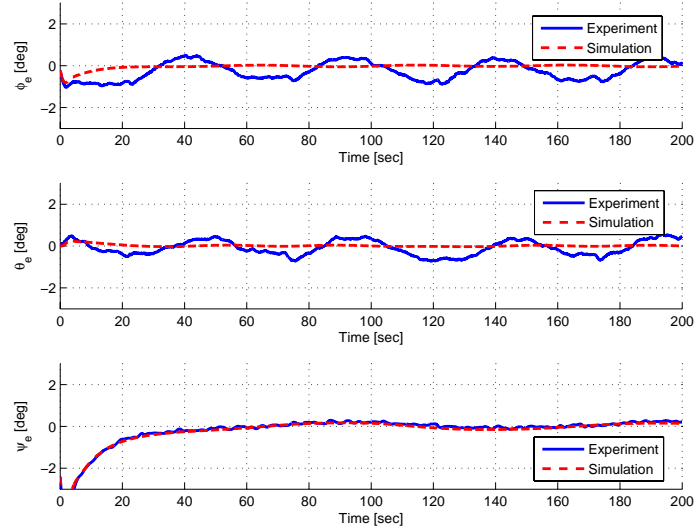


**Figure 4. Experimental and simulated results for attitude tracking error without wheel speed equalization.**

of the matrix  $C$  are shown in Figure 13. They all agree very well with the time histories predicted from numerical simulations (Figure 14).

The results from the third set of experiments are almost identical to those of the previous case, therefore we only show the plot from the time history of the wheel speeds. This is shown in Figure 15. The wheel speed equalization algorithm works as expected.

## Conclusions

In this paper we present results from the experimental validation of a control algorithm for simultaneous attitude and power tracking using a cluster of VSCMGs. A weighted minimum-norm solution for the steering logic is used, in conjunction with two wheel speed equalization algorithms. The experimental results correlate very well with numerical simulations. The small discrepancies observed in the attitude tracking error are due to the misalignment of the center of rotation of the platform and its center of mass and can be taken care of by integral action and/or by adaptive cancelation of this constant term, thus achieving even more precise attitude tracking. This is the first time where 3-axis attitude tracking with simultaneous power management has been demonstrated experimentally, as far as the authors know.

## References

- <sup>1</sup>Roes, J. B., *An Electro-Mechanical Energy Storage System for Space Application*, Vol. 3 of *Progress in Astronautics and Rocketry*, Academic Press, New York, 1961, pp. 613–622.
- <sup>2</sup>Anderson, W. and Keckler, C., “An Integrated Power/Attitude Control System (IPACS) for Space Application,” *Proceedings of the 5th IFAC Symposium on Automatic Control in Space*, Vol. 5, No. 3, 1973, pp. 991–995.

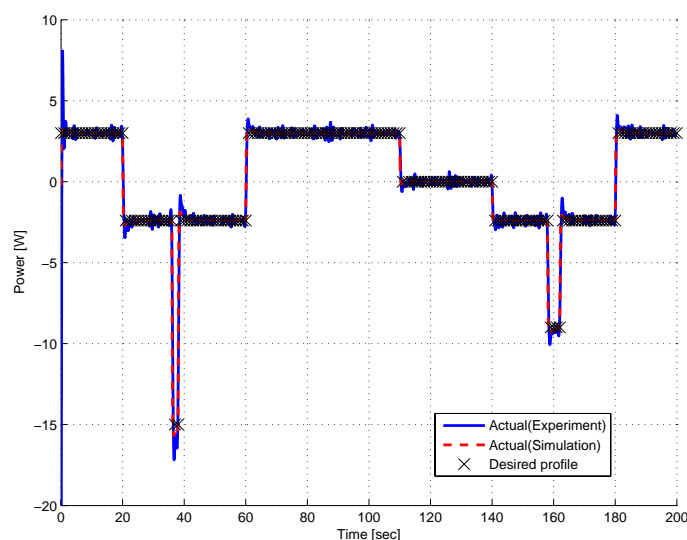


**Figure 5. Experimental and simulated results for power profile without wheel speed equalization.**

<sup>3</sup>Notti, J., Cormack III, A., Schmill, W., and Klein, W., “Integrated Power/Attitude Control System (IPACS) Study: Volume II–Conceptual Designs,” *NASA Technical Report, CR-2384*, 1974.

<sup>4</sup>Tsiotras, P., Shen, H., and Hall, C., “Satellite Attitude Control and Power Tracking with Momentum Wheels,” *Journal of Guidance, Control, and Dynamics*, Vol. 24, No. 23–34, 2001.

<sup>5</sup>Hall, C. D., “High-Speed Flywheels for Integrated Energy Storage and Attitude Control,” *Proceedings of the American Control Conference*, Vol. 3, June 4–6, 1997, pp. 1894–1898, Albuquerque, NM.

<sup>6</sup>Caswell, P., “Getting Flywheels Ready to Fly,” *GRC News Release 00-017*, March 2000.

<sup>7</sup>Roithmayr, C. M., Karlgaard, C. D., Kumar, R. R., and Bose, D. M., “Integrated Power and Attitude Control with Spacecraft Flywheels and Control Moment Gyroscopes,” *Journal of Guidance, Control, and Dynamics*, Vol. 27, No. 5, 2004, pp. 859–873.

<sup>8</sup>Yoon, H. and Tsiotras, P., “Spacecraft Adaptive Attitude and Power Tracking with Variable Speed Control Moment Gyroscopes,” *Journal of Guidance, Control and Dynamics*, Vol. 25, No. 6, 2002, pp. 1081–1090.

<sup>9</sup>Shuster, M. D., “A Survey of Attitude Representation,” *Journal of the Astronautical Sciences*, Vol. 41, No. 4, 1993, pp. 439–517.

<sup>10</sup>Tsiotras, P., “Stabilization and Optimality Results for the Attitude Control Problem,” *Journal of Guidance, Control, and Dynamics*, Vol. 19, No. 4, 1996, pp. 772–779.

<sup>11</sup>Schaub, H. and Junkins, J. L., “Stereographic Orientation Parameters for Attitude Dynamics: A Generalization of the Rodrigues Parameters,” *Journal of the Astronautical Sciences*, Vol. 44, No. 1, 1996, pp. 1–19.

<sup>12</sup>Schaub, H., Vadali, S. R., and Junkins, J. L., “Feedback Control Law for Variable Speed Control Moment Gyroscopes,” *Journal of the Astronautical Sciences*, Vol. 46, No. 3, 1998, pp. 307–328.

<sup>13</sup>Margulies, G. and Aubrun, J. N., “Geometric Theory of Single-Gimbal Control Moment Gyro Systems,” *Journal of the Astronautical Sciences*, Vol. 26, No. 2, 1978, pp. 159–191.

<sup>14</sup>Bedrossian, N. S., Paradiso, J., Bergmann, E. V., and Rowell, D., “Steering Law Design for Redundant Single-Gimbal Control Moment Gyroscopes,” *Journal of Guidance, Control, and Dynamics*, Vol. 13, No. 6, 1990, pp. 1083–1089.

<sup>15</sup>Ford, K. A. and Hall, C. D., “Singular Direction Avoidance Steering for Control-Moment Gyros,” *Journal of Guidance, Control, and Dynamics*, Vol. 23, No. 4, 2000, pp. 648–656.

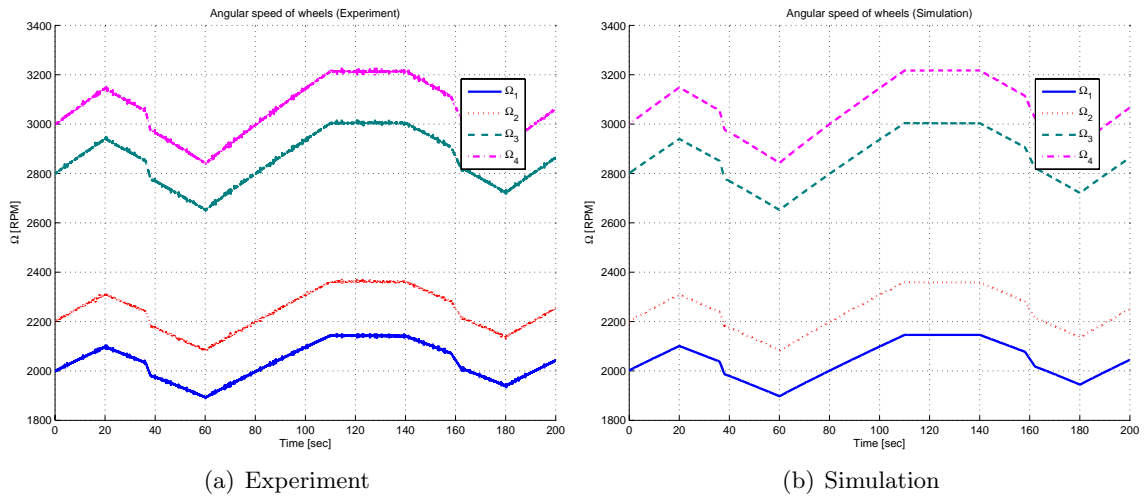


**Figure 6. Wheel speed history without wheel speed equalization.**

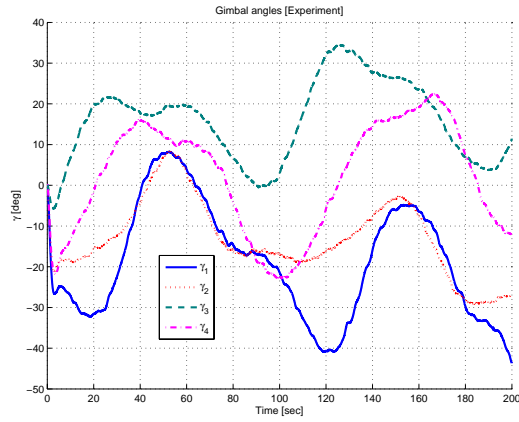
<sup>16</sup>Schaub, H. and Junkins, J. L., “Singularity Avoidance Using Null Motion and Variable-Speed Control Moment Gyros,” *Journal of Guidance, Control, and Dynamics*, Vol. 23, No. 1, 2000, pp. 11–16.

<sup>17</sup>Wie, B., “Singularity Escape/Avoidance Steering Logic for Control Moment Gyro Systems,” *Journal of Guidance, Control, and Dynamics*, Vol. 28, No. 5, 2005, pp. 948–956.

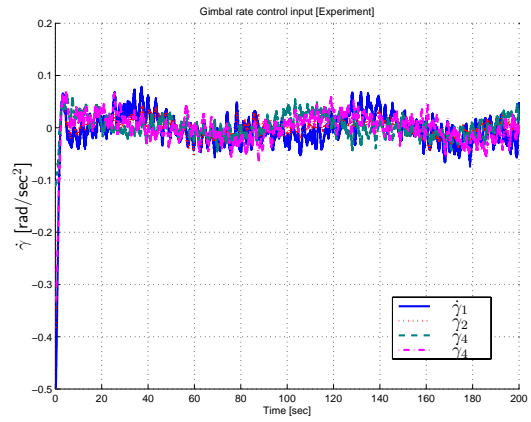
<sup>18</sup>Jung, D. and Tsiotras, P., “An Experimental Comparison of CMG Steering Control Laws,” *AIAA/AAS Astrodynamics Specialist Conference and Exhibit*, Providence, RI, 2004, AAS Paper 2004-5294

<sup>19</sup>Mathworks, “xPC Target User’s Guide,” On-line document, <http://www.mathworks.com/>, 2001.

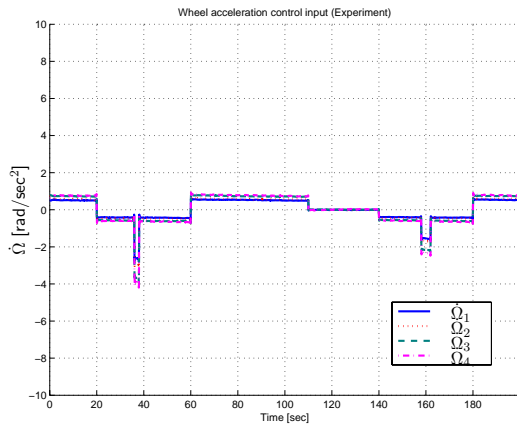
<sup>20</sup>Jung, D. and Tsiotras, P., “A 3-DoF Experimental Test-Bed for Integrated Attitude Dynamics and Control Research,” *AIAA Guidance, Navigation, and Control Conference*, Austin, Texas, 2003, AIAA Paper 2003-5331.



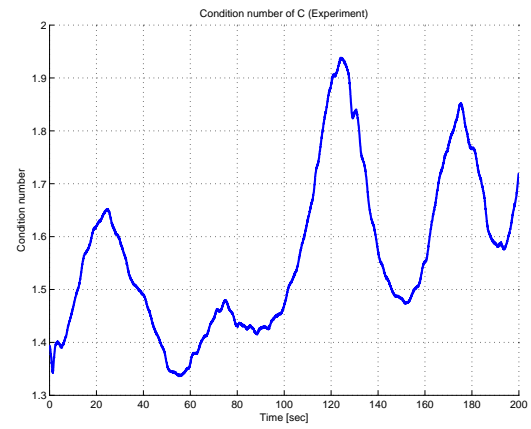
(a) Gimbal angles



(b) Gimbal rate control input

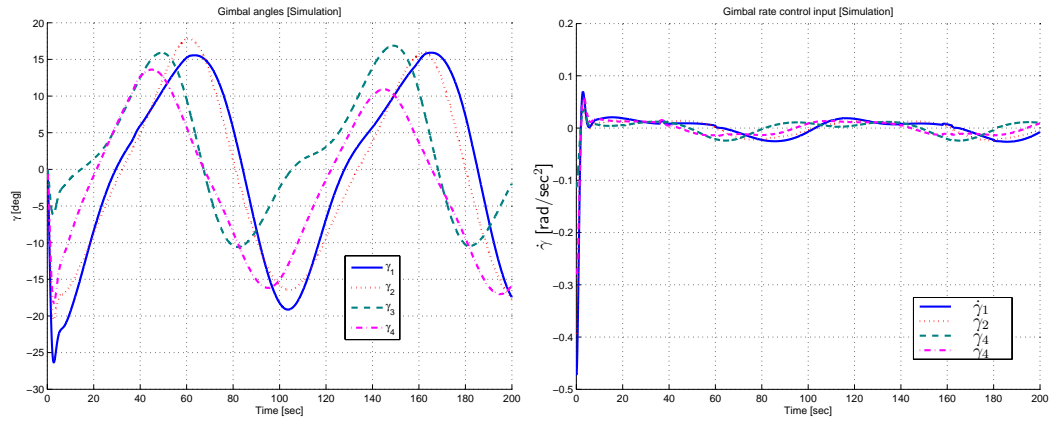


(c) Wheel acceleration control input



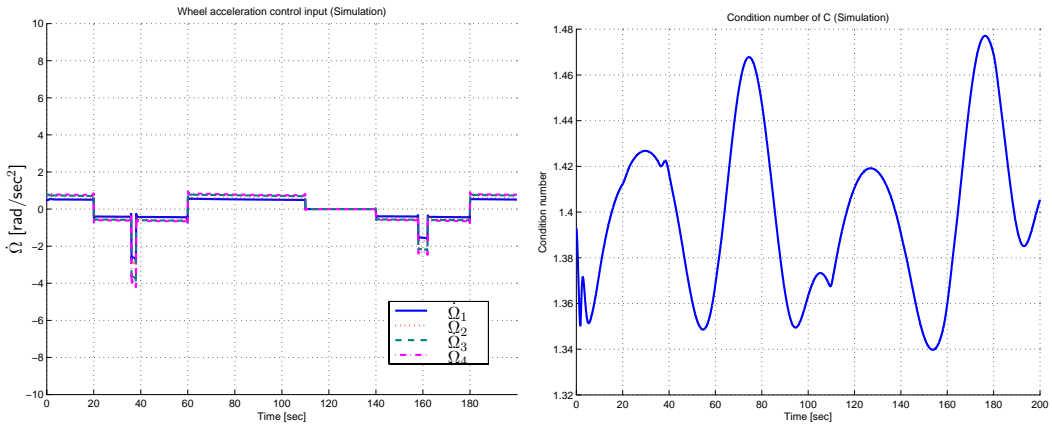
(d) Condition number of  $C$

**Figure 7. History of gimbal angles, control inputs, and condition number of matrix  $C$  without wheel speed equalization [Experiment].**



(a) Gimbal angles

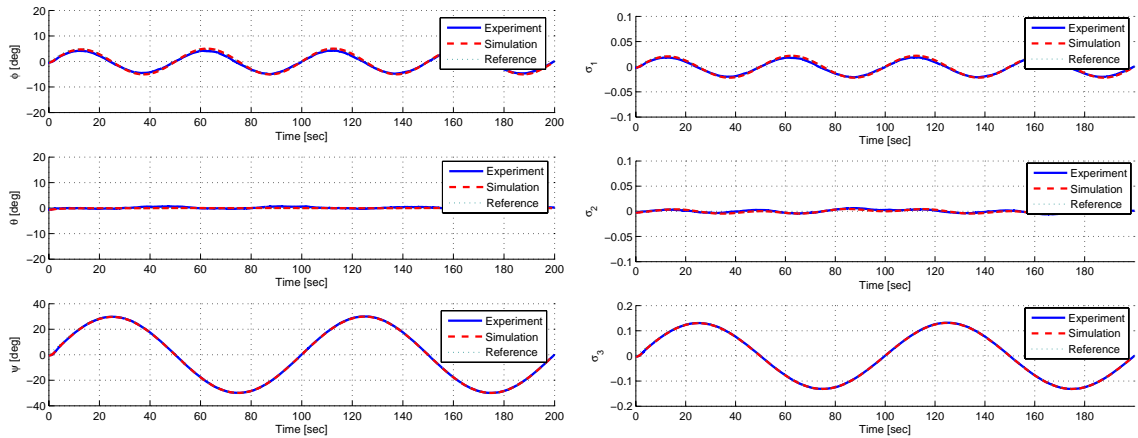
(b) Gimbal rate control input



(c) Wheel acceleration control input

(d) Condition number of  $C$

**Figure 8. History of gimbal angles, control inputs, and condition number of matrix  $C$  without wheel speed equalization [Simulation].**



(a) Euler angles

(b) MRPs

**Figure 9. Experimental and simulated results for attitude with first wheel speed equalization algorithm.**

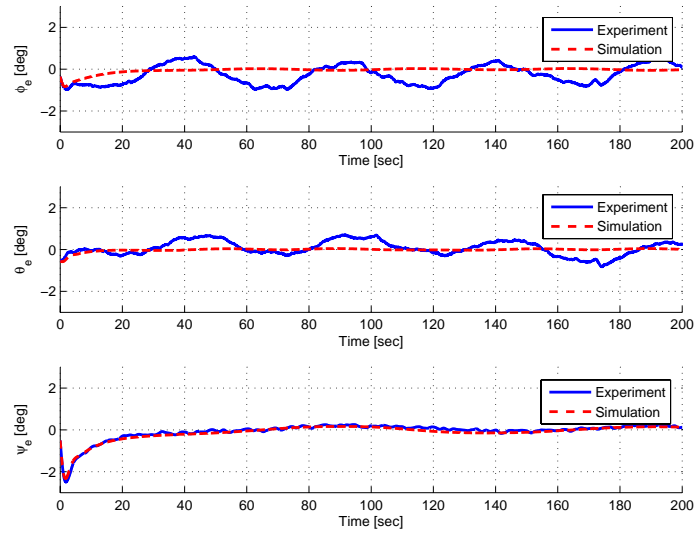


Figure 10. Experimental and simulated results for attitude tracking error with first wheel speed equalization algorithm.

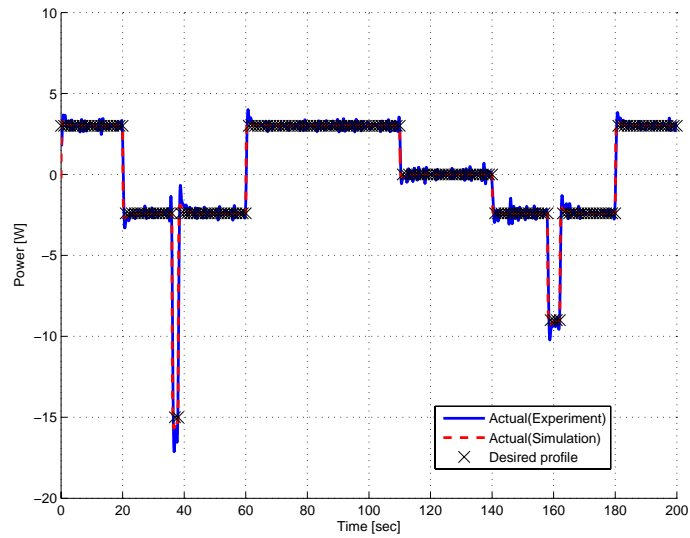


Figure 11. Experimental and simulated results for power profile with first wheel speed equalization algorithm.

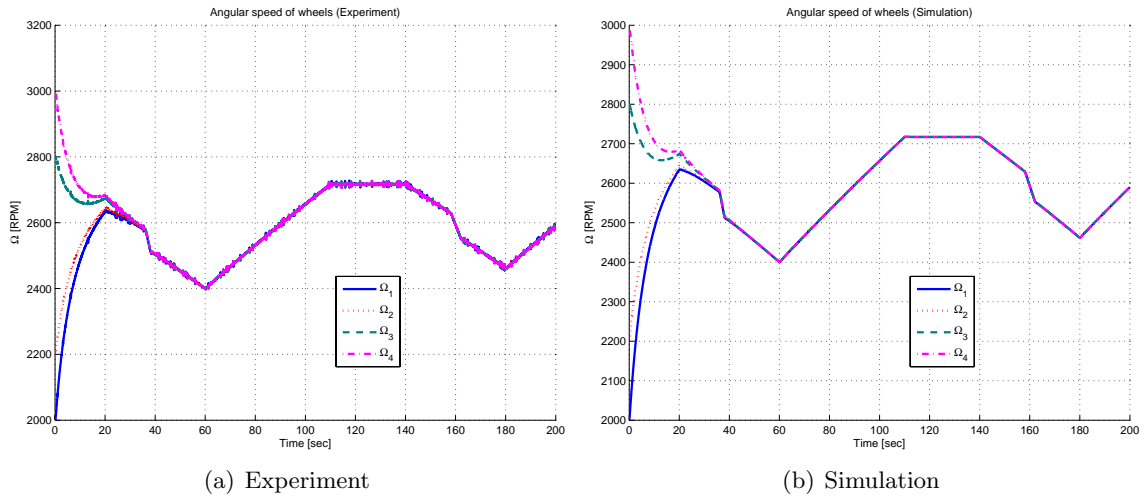


Figure 12. Wheel speed history with first wheel speed equalization algorithm engaged.

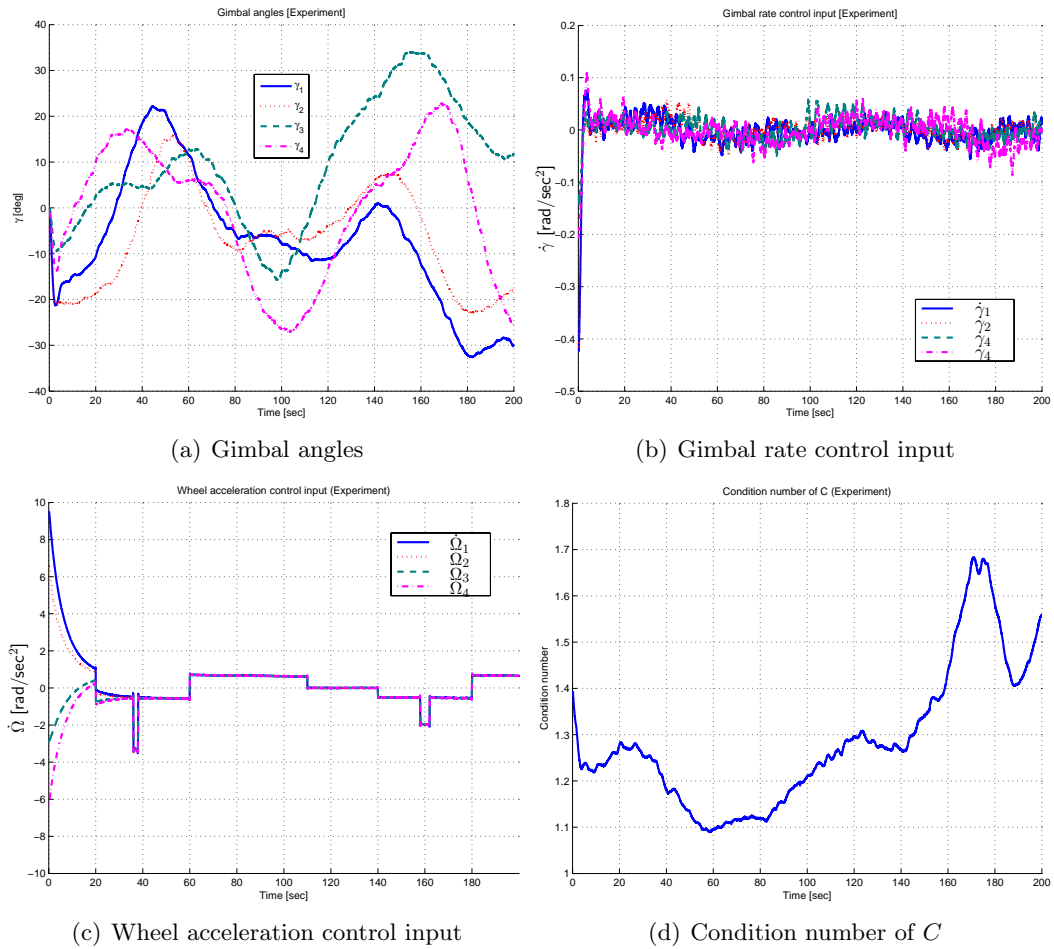
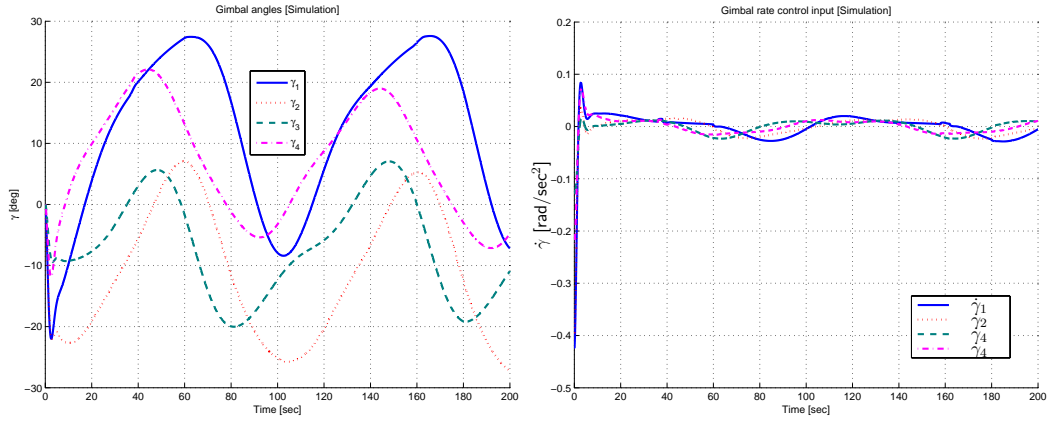
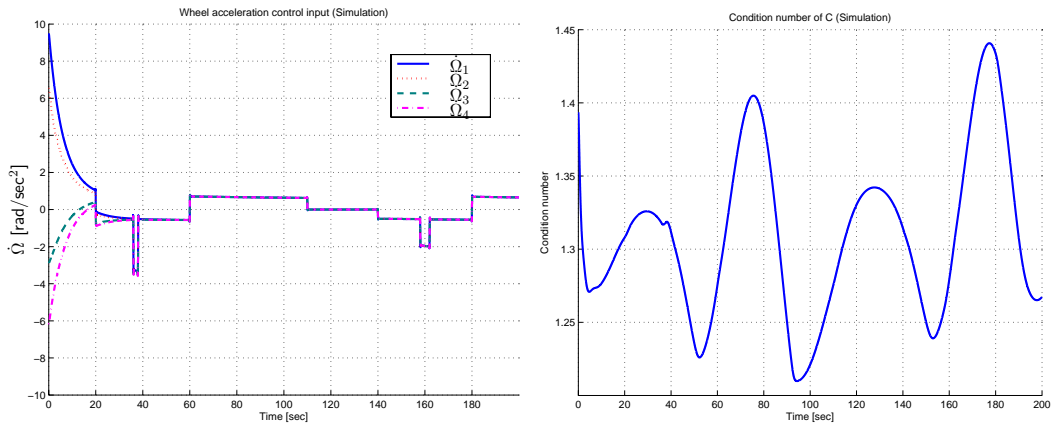


Figure 13. History of gimbal angles, control inputs, and condition number of matrix  $C$  with first wheel speed equalization algorithm [Experiment].



(a) Gimbal angles

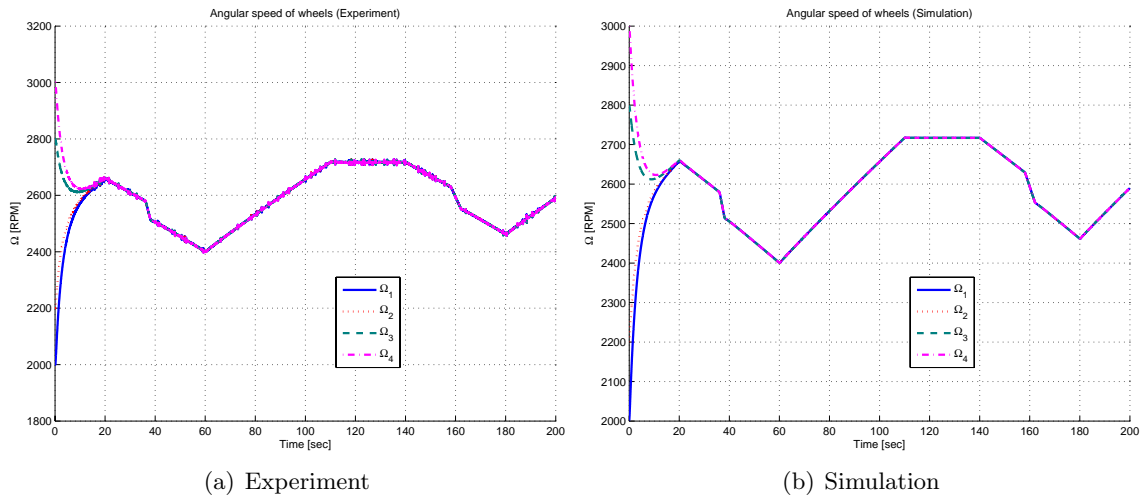
(b) Gimbal rate control input



(c) Wheel acceleration control input

(d) Condition number of  $C$

Figure 14. History of gimbal angles, control inputs, and condition number of matrix  $C$  with first wheel speed equalization algorithm [Simulation].



(a) Experiment

(b) Simulation

Figure 15. Wheel speed history with second wheel speed equalization algorithm engaged.